RSC Advances

PAPER

Cite this: *RSC Adv.*, 2021, **11**, 2066

$LiYF_4$-nanocrystal-embedded glass ceramics for upconversion: glass crystallization, optical thermometry and spectral conversion

Xinyue Li, *[ac] Liting Qiu,*[b] Youli Chen,*[a] Yiwen Zhu,*[a] Hua Yu,*[a] Jiasong Zhong, *[a] Tao Yang[a] and Qinan Mao[a]

Received 28th September 2020
Accepted 16th December 2020

DOI: 10.1039/d0ra08285f

rsc.li/rsc-advances

Glass ceramics (GCs) can perfectly integrate nanocrystals (NCs) into bulk materials. Herein, GCs containing $LiYF_4$ NCs were fabricated *via* a traditional melt-quenching method and subsequent glass crystallization. Structural characterization was carried out *via* X-ray diffraction (XRD), transmission electron microscopy (TEM), selected area electron diffraction (SAED), and scanning transmission electron microscopy high-angle annular dark-field (STEM-HAADF) analysis, suggesting the precipitation of $LiYF_4$ NCs from a glass matrix. Taking Eu^{3+} as a structural probe, the spectrographic features provide compelling evidence for the partition of dopants. In particular, intense upconversion (UC) emission was achieved when co-doped with Yb^{3+} and Er^{3+}. Temperature-dependent UC emission behaviour was also established based on the fluorescence intensity ratio (FIR) of Er^{3+}, to study its properties for optical thermometry. Furthermore, spectral conversion was attained through cross relaxation (CR) between Ce^{3+} and Ho^{3+}, tuning from green to red with various Ce^{3+} doping concentrations. There is evidence that $LiYF_4$ NC-embedded GCs were favorable for UC, which may be extremely promising for optical thermometry and spectral conversion applications. This work may open up new avenues for the exploration of GC materials for expansive applications.

1. Introduction

UC, which converts low-energy-photons into high-energy-photons, is an anti-stock process. Benefitting from their characteristic of ladder-like energy levels and relatively long lifetimes, trivalent lanthanide ions are extremely favourable for UC. As a consequence, lanthanide-doped UC luminescent materials, especially NCs, have been attracting attention recently, owing to their diverse prospects in optical amplifiers, lighting, three-dimensional (3-D) volumetric displays, bioimaging, anti-counterfeiting, laser devices, optical thermometry and so on.[1–10] In general, NCs with remarkable UC performance have been elaborately designed, and need complicated preparation technology and expensive ingredients.

Glass can be an ideal bulk medium for NCs, on account of its ease of synthesis and high-stability features. These composite bulk materials, which integrate the intriguing merits of glasses and NCs, are called GCs, and they have been considered a new class of preeminent luminescent materials with wide application.[11–16] In particular, oxyfluoride GCs, which means that fluorides are precipitated *in situ* from oxide glasses, are at the forefront of GC materials, since they provide a local field environment with low phonon energy for lanthanide doping ions. Indeed, fluorides are characterized by low phonon frequencies (<350 cm^{-1}),[17] avoiding adverse non-radiative relaxation processes; thus they could be considered ideal hosts for luminescence. Therefore, various oxyfluoride GCs containing fluoride NCs are continuously being explored: for instance CaF_2, YF_3, $KMnF_3$, $NaYF_4$, $BaGdF_5$, and $NaYb_2F_7$ NCs.[18–23]

Among various fluorides, hexagonal $NaLnF_4$, a typical representative fluoride, was initially considered as one of the most efficient green UC host materials when doped with Yb/Er.[24] In fact, a high quantum yield of 5.0% was achieved by Chen and co-workers in $LiLuF_4$: Yb, Er@$LiLuF_4$ core/shell nanoparticles.[25] In 2011, Prasad reported a four times higher quantum yield in Yb/Er codoped $LiYF_4$ nanoparticles, compared to that of $NaYF_4$ nanoparticles.[26] Since then, $LiLnF_4$ has caught immense interest and become a research hotspot.[27–30] According to the crystal structure of $LiYF_4$ in Fig. 1(a), it evidences a tetragonal structure belonging to an $I4_1/a$ space group.[31] There exist several polyhedral structures involving tetrahedral structures composed of Li^+ and F^- and octahedral structure consisting of Y^{3+} and F^-.

[a]*College of Materials & Environmental Engineering, Hangzhou Dianzi University, Hangzhou 310018, China. E-mail: lixy@hdu.edu.cn*

[b]*Key Laboratory of Strongly-Coupled Quantum Matter Physics, Chinese Academy of Sciences, School of Physical Sciences, University of Science and Technology of China, Hefei 230026, China*

[c]*Fujian Provincial Key Laboratory of Quantum Manipulation and New Energy Materials, Fuzhou 350117, China*

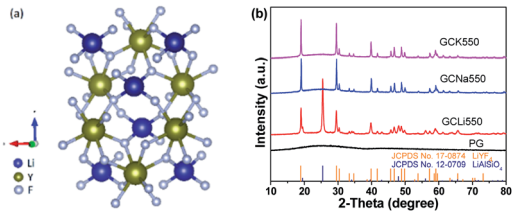

Fig. 1 (a) The crystal structure of tetragonal $LiYF_4$. The blue, golden, and grey balls represent Li, Y, and F, respectively. (b) The XRD patterns of PG and GC samples with standard PDF cards (JCPDS no. 17-0874 $LiYF_4$ and JCPDS no. 12-0709 $LiAlSiO_4$).

Yet the synthesis of GC materials has depended greatly on practice, and applicable principles of glass crystallization need to be urgently explored. Therefore, it is still a great challenge to precipitate specific NCs from a glass matrix. Moreover, continuously expanding our understanding of glass crystallization for desirable GC materials needs to be complemented with a better grasp of their optical properties. The aim of this paper is to discuss the precipitation of $LiYF_4$ NCs influenced by alkali metal oxides in aluminosilicate glasses, and their UC properties for potential applications in optical thermometry and spectral conversion.

2. Experimental

2.1 Materials and synthesis

A series of chemical compositions with different alkali metal oxides (Li_2O, Na_2O, K_2O) were elaborately designed as SiO_2–Al_2O_3–Li_2O–KF–YF_3, SiO_2–Al_2O_3–Na_2O–KF–YF_3 and SiO_2–Al_2O_3–K_2O–KF–YF_3, as tabulated in Table 1. The total mole content of glass composition was set to 100% for easier comparison. Taking the Yb/Ho/Ce system as an example, the doping lanthanide ions, such as Yb^{3+}, Ho^{3+}, or Ce^{3+}, were introduced to substitute the sites of Y^{3+} due to their similar valence states and ionic radii, as tabulated in Table 2. The GC samples were prepared *via* a traditional melt-quenching method with subsequent heat-treatment, and were marked as GCLi, GCNa and GCK, respectively. The raw materials of SiO_2, Al_2O_3, Li_2CO_3, Na_2CO_3, K_2CO_3, LiF (A. R., all from Shanghai Macklin Biochemical Co., Ltd., Shanghai, China) and LnF_3 (Ln = Y, Yb, Er, Ce, Ho, 99.99%, all from AnSheng Inorganic Materials Co., Ltd, Jiangxi, China) were precisely weighed and ground, and the homogenous mixture was maintained at 1450 °C for 45 min in a covered corundum crucible. The melt was poured onto a copper plate preheated at 300 °C and then pressed by another copper plate. The formed precursor glasses (PGs) were maintained at 400 °C to release internal stress. During glass crystallization, the PGs were heated at 500 °C or 550 °C for 2 h to gain GC samples, marked GC500 and GC550, respectively. The PG and GC samples were cut and polished for further characterization.

Table 1 The chemical compositions of GC samples

Sample	Chemical composition
GCLi	$40SiO_2$–$25Al_2O_3$–$5Li_2O$–20KF–$10YF_3$
GCNa	$40SiO_2$–$25Al_2O_3$–$5Na_2O$–20KF–$10YF_3$
GCK	$40SiO_2$–$25Al_2O_3$–$5K_2O$–20KF–$10YF_3$

Table 2 The chemical compositions of Yb/Ho/Ce tri-doped $LiYF_4$-NC-embedded GC samples

Sample	SiO_2	Al_2O_3	K_2O	LiF	YF_3	YbF_3	HoF_3	CeF_3
GC0Ce	40	25	5	20	7.9	2	0.1	0
GC3Ce	40	25	5	20	7.6	2	0.1	0.3
GC5Ce	40	25	5	20	7.4	2	0.1	0.5
GC10Ce	40	25	5	20	6.9	2	0.1	1
GC15Ce	40	25	5	20	6.4	2	0.1	1.5
GC20Ce	40	25	5	20	5.9	2	0.1	2

2.2 Characterization

The non-crystalline and crystalline phases of the PG and GC samples were identified by XRD (MiniFlex 600 RIGAKU) with nickel-filtered Cu Kα radiation ($\lambda = 0.15418$ nm) in the 2θ range from 10° to 80°. In order to characterize the morphologies of the GC samples, TEM (JEM-2010) and SAED were employed. Furthermore, STEM operated in the HAADF mode was also performed. Moreover, the UC emission spectra and decay curves were conducted with an Edinburgh Instruments FS5 spectrofluorometer, equipped with a continuous and pulsed 980 nm laser. In order to record temperature-dependent UC emission spectra, the GC sample was loaded onto a copper host equipped with a temperature controller (OMRON E5CC-800). The temperature range was controlled from 303 K to 563 K, utilizing a type-K thermocouple and a heating tube.

3. Results and discussion

3.1 Structural characterization

Fig. 1(b) exhibits the XRD patterns of the PG and GC samples. For the PG sample, the diffraction peak was amorphous, exhibiting the random arrangement in glass. Notably, the XRD patterns of all PG samples are amorphous, and are not listed here. As a comparison, it can be directly found that several sharp diffraction peaks assigned to crystals appear superposed

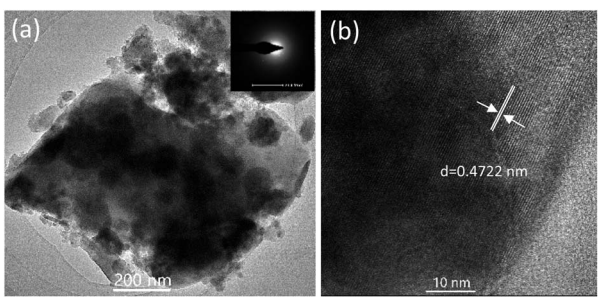

Fig. 2 (a) TEM and (b) HRTEM images of the GC550 sample. The inset in (a) presents the SAED pattern.

on the amorphous hump after glass crystallization. Corresponding to the standard PDF cards, the diffraction peaks of the GCNa550 and GCK550 samples can be indexed to tetragonal $LiYF_4$ (JCPDS no. 17-0874), verifying the successful precipitation of $LiYF_4$ NCs in aluminosilicate glasses. While the diffraction peaks of GCLi550 can be matched with not only tetragonal $LiYF_4$ but also hexagonal $LiAlSiO_4$ (JCPDS no. 12-0709), suggesting that dual NCs including fluorides and oxides have been precipitated in the glass matrix. It has been demonstrated that alkali metal ions locate outside the glass network structure, playing a significant role in breaking the bonds of the glass network and providing opportunities for glass crystallization. Accordingly, for the GCNa and GCK samples, Na^+ or K^+ act as a bond breaker, leading to preferential precipitation of Li^+ from the glass matrix. In contrast, for the GCLi sample, excess Li^+ ions were precipitated concurrently with Si^{4+} and Al^{3+}, forming $LiAlSiO_4$ NCs. It can be concluded that the addition of Na_2O or K_2O can help to break the bonds of the glass network and reduce the tendency for glass crystallization, in comparison with that of Li_2O. Apart from these, the incorporation of lanthanide ions, such as Er^{3+}, Ho^{3+} or Ce^{3+}, would not change the crystalline phases, and they are not exhibited here. In what follows, the discussion on $LiYF_4$ NC embedded GCs with different Yb/Er and Yb/Ho/Ce dopants refers to the GCK samples.

In order to give an insight into the microstructure of GCs, morphological characterization was performed; see Fig. 2. As presented by the TEM image in Fig. 2(a), the precipitated $LiYF_4$ NCs were roughly spherical with little agglomerations ranging from tens to hundreds of nanometers. Moreover, the corresponding SAED pattern in the inset shows several diffraction rings of tiny NCs, confirming the crystallinity of the $LiYF_4$ nanocrystals. Notably, there are well-demarcated lattice fringes in the HRTEM image in Fig. 2(b). The corresponding interplanar spacing d is given as 0.4722 nm, which matches perfectly with the (101) lattice plane of tetragonal $LiYF_4$. Furthermore, STEM-HAADF was also employed to examine the element distribution. In Fig. 3, there is evidence that elements Y, Yb, Er are enriched in $LiYF_4$ NCs, while elements Si, Al, O, K are maintained in glass. Notably, the element F fills in both NCs and glass. Consequently, these results confirm the successful precipitation of $LiYF_4$ NCs in aluminosilicate glasses, as well as the partition of dopants.

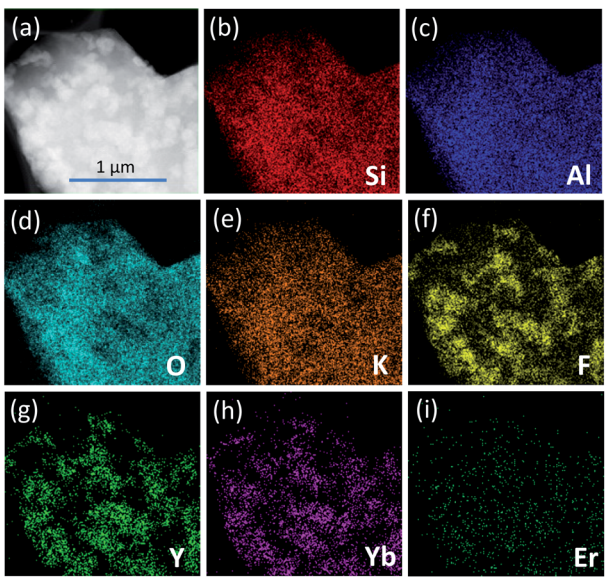

Fig. 3 (a) STEM-HAADF images of the GC550 sample with (b) Si, (c) Al, (d) O, (e) K, (f) F, (g) Y, (h) Yb, and (i) Er elemental mapping.

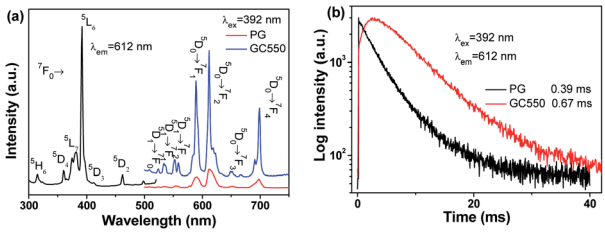

Fig. 4 (a) Excitation and emission spectra and (b) decay curves of Eu^{3+}-doped PG and GC550 samples.

Eu^{3+}, which serves as a fluorescent probe, was introduced into the GC samples to examine the local field environment before and after glass crystallization, as shown in Fig. 4. When monitored at 612 nm, the excitation spectrum was recorded with typical excitation bands centered at 315 nm, 360 nm, 381 nm, 392 nm, 413 nm and 462 nm of Eu^{3+}, which are ascribed to the transitions from the ground $^7F_0$ state to the upper $^5H_6$, $^5D_4$, $^5L_7$, $^5L_6$, $^5D_3$ and $^5D_2$ states, respectively. Furthermore, Fig. 4(a) also depicts the emission spectra of the PG and GC550 samples. Under excitation at 392 nm, several distinct emission bands of Eu^{3+} are composed of 524 nm, 533 nm, 552 nm, 589 nm, 612 nm, 649 nm and 699 nm, attributed to the $^5D_1 \rightarrow {}^7F_0$, $^5D_1 \rightarrow {}^7F_1$, $^5D_1 \rightarrow {}^7F_2$, $^5D_0 \rightarrow {}^7F_1$, $^5D_0 \rightarrow {}^7F_2$, $^5D_0 \rightarrow {}^7F_3$, and $^5D_0 \rightarrow {}^7F_4$ transitions, respectively. It is worth noting that dramatically enhanced and narrowed peaks for the GC550 sample and typical glass-like inhomogeneous broadening peaks for PG emerge, indicating the ordered local field environment of Eu^{3+} in the GC550 sample and the disordered field of PG. Impressively, the intensity ratio between the electric dipolar $^5D_0 \rightarrow {}^7F_2$ transition and the magnetic dipolar $^5D_0 \rightarrow {}^7F_1$ transition decreases after glass crystallization.[32] Furthermore, Fig. 4(b) plots the luminescence decay curves of Eu^{3+}, monitored at 612 nm. The lifetimes of the PG and GC550 samples are estimated at 0.39 ms and 0.67 ms, respectively. In comparison with that of PG, the elongated lifetime of GC offers further evidence for the partition of Eu^{3+} into $LiYF_4$ NCs. Overall, we can conclude that dopants would be partitioned into NCs with superior optical properties after glass crystallization, owing to the low-photon-energy and ordered local field surroundings of the fluoride NCs.

3.2 UC emission

To investigate the UC mechanism of the Yb/Er system, the UC behaviours of the PG and GC samples were recorded and are shown in Fig. 5. Under excitation at 980 nm, distinct UC

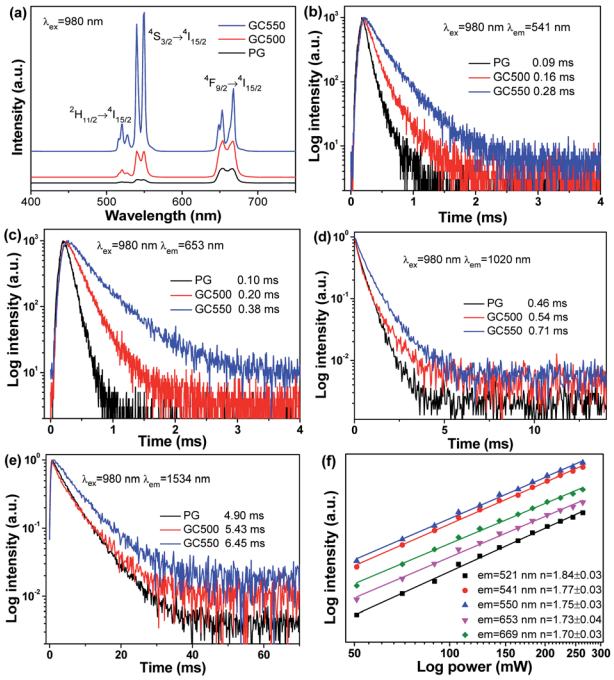

Fig. 5 (a) UC emission spectra and decay curves monitored at (b) 541 nm, (c) 654 nm, (d) 1020 nm, and (e) 1534 nm from PG and GC samples. (f) The dependence of UC intensity on pump power for the GC550 sample.

emission bands of Er^{3+} can be observed in Fig. 5(a). The green UC emissions, involving emission bands centered at 521 nm, 541 nm and 550 nm, are dominant. They originate from the transitions of $^2H_{11/2} \rightarrow {}^4I_{15/2}$ and $^4S_{3/2} \rightarrow {}^4I_{15/2}$, respectively. In addition, the red UC emissions centered at 653 nm and 669 nm are assigned to the transition of $^4F_{9/2} \rightarrow {}^4I_{15/2}$. It is worth noting that the UC emission intensities could be enhanced, and the Stark splitting is also particularly obvious for the GC samples, compared to that of PG. For PG, the disordered local field surroundings of the luminescent centers act against UC emission, while after glass crystallization the ordered field with low photon energy benefits UC. In addition, the amount of dopants incorporated into $LiYF_4$ NCs also increases with the growth of NCs, when the temperature of the heat treatment rises. Hence, the emission intensities of GC550 are also enhanced, compared to that of GC500. Correspondingly, the decay curves were also measured in Fig. 5(b–e), monitored at 541 nm, 653 nm, 1020 nm and 1534 nm. The fitting lifetimes of green UC emission were obtained as 0.09 ms for PG, 0.16 ms for GC500 and 0.28 ms for GC550. Evidently elongated lifetimes could be obtained during glass crystallization, which is consistent with the UC emission spectra. The occasions of red UC emission at 653 nm and infrared emission at 1020 nm and 1534 nm are similar, as exhibited in Fig. 5(c–e), respectively. All these findings indicate that the dopants of Yb^{3+} and Er^{3+} have been successfully partitioned into $LiYF_4$ NCs.

Furthermore, the dependence of UC intensities on pump power was investigated. According to previous studies,[33] it is

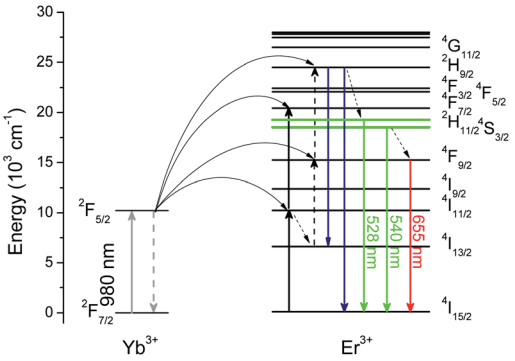

Fig. 6 Energy levels diagrams for Yb^{3+} and Er^{3+} and possible UC routes.

suggested that the relationship between UC intensity I and pump power P can be given as follows:

$$I \propto P^n \quad (1)$$

where n represents the number of photons for UC emission. Double logarithmic plots are plotted in Fig. 5(d). The slopes of green UC emissions located at 521 nm, 541 nm and 550 nm are obtained as 1.84 ± 0.03, 1.77 ± 0.03, and 1.75 ± 0.03, respectively, indicating a two-photon process for green UC emissions. In addition, the values of n are 1.73 ± 0.03 and 1.70 ± 0.03, when monitoring red UC emissions centered at 653 nm and 669 nm. As a consequence, green and red UC emissions of Yb/Er codoped $LiYF_4$ NCs originate from a two-photon process.

To provide more precise information for a better exploration of the UC mechanism, Fig. 6 illustrates the energy diagrams of Yb^{3+} and Er^{3+}, as well as the possible UC routes. When excited by 980 nm, Yb^{3+} has a larger absorption cross-section than Er^{3+}. Continuous 980 nm photons could be absorbed by Yb^{3+}, pumping from $^2F_{7/2}$ to $^2F_{5/2}$. Subsequently, the absorbed energies are transferred from Yb^{3+} to the adjacent Er^{3+}. Benefitting from the ladder-like energy levels and relatively long lifetimes of Er^{3+} ions, they can absorb the energy from Yb^{3+} successively through ground state absorption (GSA) and excited state absorption (ESA), populating the higher excited energy levels. Green UC emissions could be attained after continuous ESA and GSA, and then relax non-radiatively to $^2H_{11/2}$ and $^4S_{3/2}$ states. When referring to the red UC emissions, two primary routes are given in Fig. 6. One is the non-radiative relaxation from the $^4S_{3/2}$ state. On the other hand, a multi-phonon nonradiative relaxation process follows after absorbing a 980 nm photon by ESA, resulting in a population in the $^4I_{13/2}$ state. And then absorbing another 980 nm photon populates the $^4F_{9/2}$ state, producing red UC emissions. These results verify that a two-photon process is responsible for both green and red UC emissions of Er^{3+}, which is consistent with the obtained n from the dependence of UC emission intensities on pump power.

3.3 Temperature-dependent UC behaviours

Non-contact temperature evaluation plays a greater and greater role in daily life and technology fields, especially in today's

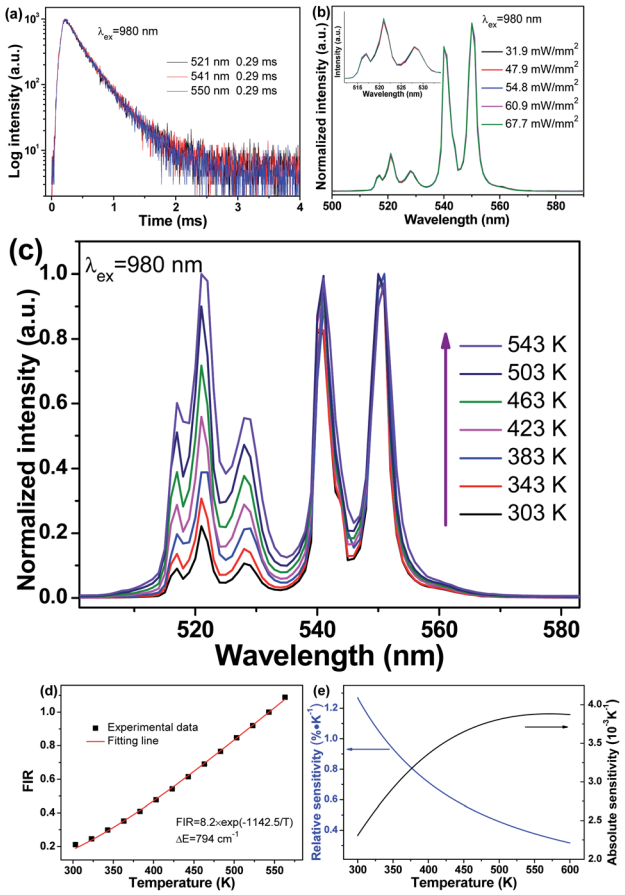

Fig. 7 (a) Decay curves monitored at 521 nm, 541 nm, and 550 nm at room temperature. (b) Normalized UC emission spectra under 980 nm excitation with various pump power densities. For clarity, the normalized UC emission spectra in the range of 510–538 nm are amplified in the inset. (c) Temperature-dependent UC emission spectra of the GC550 sample excited at 980 nm and 31.9 mW mm^{-2}. (d) Fitting line and experimental data showing the variation of FIR with temperature. (e) Relative sensitivity and absolute sensitivity curves.

prevention and control of COVID-19 globally. In particular, optical thermometry in terms of the fluorescence intensity ratio (FIR) method hit the spot, since it possesses unique features, such as non-invasiveness, high resolution, real-time response and gets rid of errors in measurement, such as laser fluctuations or inhomogeneous distribution of luminescent centres. For Er^{3+}, it is perfectly suitable for optical thermometry using the FIR method, benefitting from the thermal coupled energy levels (TCELs) of $^2H_{11/2}$ and $^4S_{3/2}$. Besides, the UC emissions of the two corresponding TCELs are dominant, which is helpful for future applications. When it works as a temperature sensor, the relative population of particles located at the two related TCELs obeys the Boltzmann distribution, after reaching a fairly rapid thermal equilibrium. In this case, there exists a corresponding relationship between FIR and temperature, and could be given as follows:

$$R = B\exp\left(-\frac{\Delta E}{k_B T}\right) \quad (2)$$

where R represents the value of the ratio of the transitions of $^2H_{11/2} \rightarrow {}^4I_{15/2}$ and $^4S_{3/2} \rightarrow {}^4I_{15/2}$, k_B represents the Boltzmann constant, B represents a constant, and ΔE represents the energy gap between $^2H_{11/2}$ and $^4S_{3/2}$. Fig. 7(a) plots decay curves at room temperature monitored at 521 nm, 541 nm and 550 nm. Notably, the same lifetimes could be obtained, suggesting that thermal equilibrium has already been reached at room temperature. As a consequence, it is available for optical thermometry, on the basis of the FIR method.

In addition, the heating effect by an infrared laser is also a factor which influences the performance of optical thermometry. In actual use, the heating effect would increase the temperature of the object to be measured, deviating from the actual temperature. Hence, it is of great importance to eliminate the heating effect, putting forward higher requirements for the luminescent materials. Fig. 7(b) illustrates the normalized UC emission spectra under various pump power densities of 980 nm. When excited at 980 nm whose power density is lower than 54.8 mW mm^{-2}, the spectral lines coincide perfectly, indicating no heating effect in this power density range. There may be a slight heating effect when the power density is above 60.9 mW mm^{-2}. On the premise of guaranteeing superior UC properties, 31.9 mW mm^{-2} is chosen as the pump density for excitation to eliminate the heating effect.

Following this approach, temperature-dependent behaviours were studied to examine the performance of Yb/Er codoped $LiYF_4$ NC embedded GCs as a temperature sensor, as illustrated in Fig. 7. To be more intuitive, the temperature-dependent UC emission intensities were normalized to the emission band at 550 nm, as exhibited in Fig. 7(c). Intriguingly, under excitation of 980 nm, the emission bands at 521 nm and 541 nm are dramatically enhanced in comparison with that of 550 nm, when the temperature is increasing. Correspondingly, the ratio varies with temperature, as presented in Fig. 7(d). It

Table 3 Relevant data relating to Yb–Er systems for optical thermometry uses

Yb–Er system	Temperature range (K)	Energy gap (cm^{-1})	Relative sensitivity (% K^{-1})	Ref.
TeO_2–WO_3 glasses	300–690	679	$977/T^2$	34
YF_3–BaF_2–$Ba(PO_3)_2$ glasses	77–500	390	$559/T^2$	35
$LiYF_4$ NCs	298–358	748	$1076/T^2$	36
β-$NaGdF_4$ GCs	303–563	789	$1135/T^2$	37
$LiYF_4$ GCs	303–563	794	$1142/T^2$	This work

can be observed that the fitting line originating from eqn (2) matches perfectly well with the experimental data, and the energy gap ΔE between the two related TCELs is estimated to be 794 cm^{-1}, which is consistent with previous studies.[33]

Furthermore, the performance of Yb/Er codoped $LiYF_4$ NC embedded GCs for temperature sensing could also be quantitatively evaluated by utilizing the sensitivity S. The sensitivity S_R and absolute sensitivity S_A are given as follows:

$$S_R = \left|\frac{1}{R}\frac{dR}{dT}\right| = \frac{\Delta E}{k_B T^2} \quad (3)$$

$$S_A = \left|\frac{dR}{dT}\right| = R\frac{\Delta E}{k_B T^2} \quad (4)$$

Compared to the absolute sensitivity S_A, the relative sensitivity S_R is more applicable. According to eqn (3) and (4), the sensitivity curves are plotted in Fig. 7(e). It can be seen that the maximum of the relative sensitivity S_R is achieved as 1.27% K^{-1} at 300 K, while the absolute sensitivity S_A could reach its maximum of 3.88 × 10^{-3} K^{-1} at 570 K.

In particular, several typical Yb/Er systems for optical thermometry based TCELs are listed in Table 3. It can be seen that the related relative sensitivities S_R of GCs are usually superior to those of glasses, verifying the enhanced and narrowed emission bands favouring optical thermometry. In spite of the similar relative sensitivities achieved by NCs and GCs, GCs with a stable glass network exhibit higher stabilities in comparison with NCs, which is a prominent advantage for future applications. Accordingly, Yb/Er codoped $LiYF_4$ NC embedded GCs could be a remarkable alternative for optical thermometry, on the basis of the FIR of Er^{3+}.

3.4 Spectral conversion

Furthermore, special UC emission could also be desirably manipulated through spectral conversion. As an alternative, cross relaxation (CR) turns out to be effective on account of the abundant energy levels of lanthanides. CR is a method of energy transfer: that is, one de-excited particle transfers its energy to another, making it become excited. Therefore, matched energy gaps become an indispensable prerequisite for tailoring emissions. For trivalent Ce^{3+}, it consists of a couple of energy levels $^2F_{5/2}$ and $^2F_{7/2}$, whose energy gap is about 2200 cm^{-1}. Taking the ladder-like energy levels of Ho^{3+} into consideration, it is capable of matching the energy gap with Ce^{3+}, resulting in the realization of tunable UC emission.[38–41]

Following this strategy, Ce^{3+} was introduced into Yb/Ho doped $LiYF_4$ NC embedded GCs to fulfil this spectral regulation, as displayed in Fig. 8. Fig. 8(a) illustrates the UC emission spectra without Ce^{3+}. Under irradiation of 980 nm, typical emission bands of Ho^{3+} at 536 nm, 657 nm and 750 nm were observed, corresponding to the transitions from the $^5S_2/^5F_4$, $^5F_5$ and $^5I_4$ states to the ground $^5I_8$ state, respectively. Notably, the evidently improved and sharpened UC emission bands for GC0Ce provide powerful evidence for the partition of dopants into fluoride NCs, which is extremely similar to that of Er^{3+}. In addition, it is not difficult to see that green UC emissions predominate, with green light distinguishable by the naked eye. Nevertheless, the green UC emission bands decrease while the red band increases with an increased amount of Ce^{3+}. In particular, single red light could be attained when the Ce^{3+} concentration reaches 15%. Thus, the ratios of red-to-green emission dramatically increase, as exhibited in Fig. 8(c), leading to the tuned UC emission colour ranging from green to yellow and then to red. Furthermore, decay curves were measured by monitoring at 536 nm of Ho^{3+}, as plotted in Fig. 8(d). The estimated lifetimes for the GC samples were shortened, with the addition of Ce^{3+}, verifying the existence of an energy transfer process from Ho^{3+}. It is the CR process that plays a crucial role in this spectral conversion.

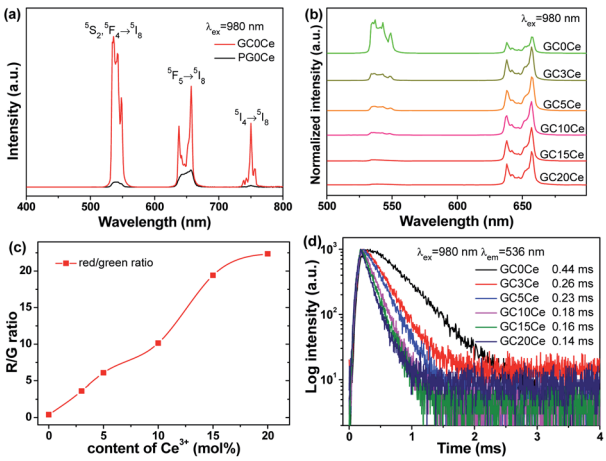

Fig. 8 (a) UC emission spectra of PG0Ce and GC0Ce samples under irradiation of 980 nm. (b) Normalized UC emission spectra, and (c) red/green ratio and (d) decay curves as a function of the Ce^{3+} content.

To give a profound insight into the mechanism of the CR process, the diagrams of energy levels involving Yb/Ho/Ce are displayed in Fig. 9. Similar to the Yb/Er system, a two-photon process is responsible for both the green and red UC emission of Ho^{3+}. Ho^{3+} can be populated into the $^5S_2/^5F_4$ states by successive GSA and ESA, producing green UC emissions. On the other hand, the Ho^{3+} in the $^5S_2/^5F_4$ states could also be populated into the $^5F_5$ state through a multiphoton nonradiative relaxation process. Alternatively, Ho^{3+} can be de-excited from

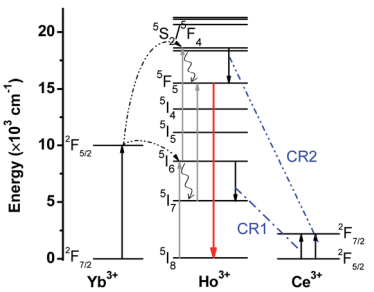

Fig. 9 Energy diagrams of Yb^{3+}, Ho^{3+}, and Ce^{3+} and their possible UC routes and CR routes.

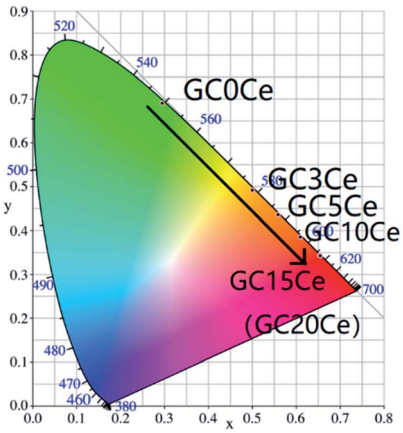

Fig. 10 The CIE diagram of GC samples with various Ce^{3+} concentrations.

Table 4 Coordinates from the CIE diagram for different samples

Sample	CIE (x, y)
GC0Ce	(0.2946, 0.6913)
GC3Ce	(0.5002, 0.4923)
GC5Ce	(0.5584, 0.4361)
GC10Ce	(0.6100, 0.3860)
GC15Ce	(0.6529, 0.3441)
GC20Ce	(0.6549, 0.3420)

the intermediate $^5I_7$ state to the lower $^5I_8$ state, and then populated by the $^5F_5$ state by absorbing 980 nm photon energy. These two possible UC routes would give rise to the red UC light. When doped with Ce^{3+}, CR processes happen. In light of the degree of matched energy gaps with Ce^{3+}, two possible CR routes are given as follows:

$$\text{CR1: } {}^5I_6(Ho^{3+}) + {}^2F_{5/2}(Ce^{3+}) \rightarrow {}^5I_7(Ho^{3+}) + {}^2F_{7/2}(Ce^{3+}); \quad (5)$$

$$\text{CR2: } {}^5S_2/{}^5F_4(Ho^{3+}) + {}^2F_{5/2}(Ce^{3+}) \rightarrow {}^5F_5(Ho^{3+}) + {}^2F_{7/2}(Ce^{3+}). \quad (6)$$

When the content of Ce^{3+} exceeds 15%, green UC emission can hardly be observed, suggesting an efficient CR process between Ho^{3+} and Ce^{3+}.

According to the obtained UC emission spectra in Fig. 8(b), the Commission International de L'Eclairage (CIE) 1931 chromaticity diagrams of the GC samples are offered in Fig. 10. With the addition of Ce^{3+}, the emission colour turns from green, to yellow, then to red. The corresponding coordinate figures are tabulated in Table 4. Therefore, tuned UC emission could be realized by an efficient CR process between Ho^{3+} and Ce^{3+}, specifically targeted to the manipulation of luminescence.

4. Conclusions

In summary, this work reported the successful precipitation of $LiYF_4$ NCs from aluminosilicate glasses with superior UC performance, as confirmed *via* structural and spectrographic characterization. Furthermore, the temperature-dependent UC behaviours *via* the FIR method in the Yb/Er system were examined, with a maximum relative sensitivity of 1.27% K^{-1} at 300 K. Moreover, spectral conversion through the CR process in the Yb/Ho/Ce system was also investigated in detail, tuning from green to red light. These findings may lead to opportunities for application in optical thermometry and light manipulation. This current study is of great importance for developing a new class of GC materials and extending the potential applications.

Conflicts of interest

There are no conflicts to declare.

Acknowledgements

This work was supported by the National Natural Science Foundation of China (51802064), and Open Fund of Fujian Provincial Key Laboratory of Quantum Manipulation and New Energy Materials (Grant No. QMNEM1904).

Notes and references

1 J. C. G. Bunzli and C. Piguet, *Chem. Rev.*, 2005, **34**, 1048–1077.
2 S. V. Eliseeva, J. C. G. Bunzli and G. Jean-Claude, *Chem. Soc. Rev.*, 2010, **39**, 189–227.
3 S. X. Wang, J. D. Lin, Y. W. He, J. K. Chen, C. B. Yang, F. Huang and D. Q. Chen, *Chem. Eng. J.*, 2020, **394**, 124889.
4 F. Wang and X. G. Liu, *Chem. Soc. Rev.*, 2009, **38**, 976–989.
5 L. Lei, H. Xia, C. K. Lim, S. Q. Xu, K. Wang, Y. P. Du and P. N. Prasad, *Chem. Mater.*, 2019, **31**, 8121–8128.
6 D. M. Yang, P. A. Ma, Z. Y. Hou, Z. Y. Cheng, C. X. Li and J. Lin, *Chem. Soc. Rev.*, 2015, **44**, 1416–1448.
7 R. R. Deng, F. Qin, R. F. Chen, W. Huang, M. H. Hong and X. G. Liu, *Nat. Nanotechnol.*, 2015, **10**, 237–242.
8 F. Vetrone, R. Naccache, A. Zamarron, A. J. de la Fuente, F. Sanz-Rodriguez, L. M. Maestro, E. M. Rodriguez, D. Jaque, J. G. Sole and J. A. Capobianco, *ACS Nano*, 2010, **4**, 3254–3258.
9 H. Huang, J. K. Chen, Y. T. Liu, J. D. Lin, S. X. Wang, F. Huang and D. Q. Chen, *Small*, 2020, **16**, 2000708.
10 E. Downing, L. Hesselink, J. Ralston and R. Macfarlane, *Science*, 1996, **273**, 1185–1189.
11 X. F. Liu, J. J. Zhou, S. F. Zhou, Y. Z. Yue and J. R. Qiu, *Prog. Mater. Sci.*, 2018, **97**, 38–96.
12 X. Y. Li, D. Q. Chen, F. Huang, G. C. Chang, J. J. Zhao, X. V. Qiao, X. H. Xu, J. C. Du and M. Yin, *Laser Photonics Rev.*, 2018, **12**, 1800030.
13 L. Calvez, H. L. Ma, J. Lucas and X. H. Zhang, *Adv. Mater.*, 2007, **19**, 129.
14 D. Q. Chen, Y. Z. Peng, X. Y. Li, J. S. Zhong, H. Huang and J. K. Cao, *ACS Appl. Mater. Interfaces*, 2019, **11**, 30053–30064.
15 D. G. Deng, S. Q. Xu, S. L. Zhao, C. X. Li, H. P. Wang and H. D. Ju, *J. Lumin.*, 2009, **129**, 1266–1270.

16 P. P. Fedorov, A. A. Luginina and A. I. Popov, *J. Fluorine Chem.*, 2015, **172**, 22–50.
17 R. Matin-Rodriguez, S. Fischer, A. Ivaturi, B. Froehlich, K. W. Kramer, J. C. Goldschmidt, B. S. Richards and A. Meijerink, *Chem. Mater.*, 2013, **25**, 1912–1921.
18 J. J. Cai, X. T. Wei, F. F. Hu, Z. M. Cao, L. Zhao, Y. H. Chen, C. K. Duan and M. Yin, *Ceram. Int.*, 2016, **42**, 13990–13995.
19 X. Y. Li, L. Y. Yang, Y. W. Zhu, J. S. Zhong and D. Q. Chen, *RSC Adv.*, 2019, **9**, 7948–7954.
20 F. F. Hu, J. K. Cao, X. T. Wei, X. Y. Li, J. J. Cai, H. Guo, Y. H. Chen, C. K. Duan and M. Yin, *J. Mater. Chem. C*, 2016, **4**, 9976–9985.
21 D. Q. Chen, Z. Y. Wan, Y. Zhou, X. Z. Zhou, Y. L. Yu, J. S. Zhong, M. Y. Ding and Z. G. Ji, *ACS Appl. Mater. Interfaces*, 2015, **7**, 19484–19493.
22 Z. G. Gao, K. L. Lu, X. S. Lu, X. B. Li, Z. Y. Han, S. Guo, L. Liu, F. He, P. P. Yang and J. Ren, *Opt. Lett.*, 2019, **44**, 2959–2961.
23 F. F. Hu, S. Q. Lu, Y. C. Jiang, R. F. Wei, H. Guo and M. Yin, *J. Lumin.*, 2020, **220**, 116971.
24 S. Fischer, N. D. Bronstein, J. K. Swabeck, E. M. Chan and A. P. Alivisatos, *Nano Lett.*, 2016, **16**, 7241–7247.
25 P. Huang, W. Zheng, S. Zhou, D. Tu, Z. Chen, H. Zhu, R. Li, E. Ma, M. Huang and X. Chen, *Angew. Chem., Int. Ed.*, 2014, **53**, 1252–1257.
26 G. Y. Chen, T. Y. Ohulchansky, A. Kachynski, H. Agren and P. N. Prasad, *ACS Nano*, 2011, **5**, 4981–4986.
27 X. Chen, W. Xu, H. W. Song, C. Chen, H. P. Xia, Y. S. Zhu, D. L. Zhou, S. B. Cui, Q. L. Dai and J. Z. Zhang, *ACS Appl. Mater. Interfaces*, 2016, **8**, 9071–9079.
28 J. B. Zhao, X. L. Zheng, E. P. Schartner, P. Lonescu, R. Zhang, T. L. Nguyen, D. Y. Jin and H. Ebendorff-Heidepriem, *Adv. Opt. Mater.*, 2016, **4**, 1507–1517.
29 X. Y. Jiang, C. Cao, W. Feng and F. Y. Li, *J. Mater. Chem. B*, 2016, **4**, 87–95.
30 W. Gao, R. B. Wang, Q. Y. Han, J. Dong, L. X. Yan and H. R. Zheng, *J. Phys. Chem. C*, 2015, **119**, 2349–2355.
31 B. Zheng, H. Cao, J. X. Hu, Z. F. Gu and Y. P. Zhang, *J. Alloys Compd.*, 2018, **768**, 150–160.
32 X. Y. Li, X. Chen, S. Yuan, S. Liu, C. Wang and D. Q. Chen, *J. Mater. Chem. C*, 2017, **5**, 10201–10210.
33 X. Y. Li, S. Yuan, F. F. Hu, S. Q. Lu, D. Q. Chen and M. Yin, *Opt. Mater. Express*, 2017, **8**, 3023–3033.
34 A. Pandey, V. K. Rai, V. Kumar, V. Kumar and H. C. Swart, *Sens. Actuators, B*, 2015, **209**, 352.
35 B. Y. Lai, L. Feng, J. Wang and Q. A. Su, *Opt. Mater.*, 2010, **32**, 1154–1160.
36 M. K. Shahzad, Y. D. Zhang, M. U. Khan, X. Sun, L. Liu and H. Y. Li, *Opt. Mater. Express*, 2018, **8**, 2321–2329.
37 D. Q. Chen, Z. Y. Wan, Y. Zhou, P. Huang, J. S. Zhong, M. Y. Ding, W. D. Xiang, X. J. Liang and Z. G. Ji, *J. Alloys Compd.*, 2015, **638**, 21–28.
38 G. Y. Chen, H. C. Liu, G. Somesfalean, H. J. Liang and Z. G. Zhang, *Nanotechnology*, 2009, **20**, 385704.
39 X. Y. Li, Z. Y. Shen, Y. W. Zhu, Z. M. Zhao, Y. Z. Peng, J. S. Zhong and T. Yang, *J. Lumin.*, 2020, **227**, 117527.
40 F. F. Hu, J. J. Zhao, O. Giraldo, W. H. Song, R. F. Wei, M. Yin and H. Guo, *J. Lumin.*, 2018, **201**, 493–499.
41 D. Q. Chen, Y. Zhou, Z. Y. Wan, Z. G. Ji and P. Huang, *Dalton Trans.*, 2015, **44**, 5288–5293.